JOURNAL OF SYNCHROTRON RADIATION
ISSN 1600-5775

Atomic pair distribution function at the Brazilian Synchrotron Light Laboratory: application to the $Pb_{1-x}La_xZr_{0.40}Ti_{0.60}O_3$ ferroelectric system

M. E. Saleta,[a,b]*‡ M. Eleotério,[b] A. Mesquita,[c] V. R. Mastelaro[d] and E. Granado[a]

[a]Instituto de Física 'Gleb Wataghin', Universidade de Campinas (UNICAMP), CEP 13083-859, Campinas (SP), Brazil, [b]Laboratório Nacional de Luz Síncrotron, Caixa Postal 6192, CEP 13084-971, Campinas (SP), Brazil, [c]Instituto Geociências and Ciências Exatas, Universidade Estadual Paulista (UNESP), Rio Claro (SP), Brazil, and [d]Instituto de Física de São Carlos, Universidade de São Paulo, CP 369, 13560-970 São Carlos (SP), Brazil. *Correspondence e-mail: martin.saleta@cab.cnea.gov.ar

Received 1 March 2017
Accepted 9 June 2017

Edited by J. F. van der Veen

‡ Permanent address: CONICET – Centro Atómico Bariloche, CNEA, 8400 S. C. de Bariloche, Río Negro, Argentina.

Keywords: atomic pair distribution function; X-ray total scattering; ferroelectric relaxor.

This work reports the setting up of the X-ray diffraction and spectroscopy beamline at the Brazilian Synchrotron Light Laboratory for performing total scattering experiments to be analyzed by atomic pair distribution function (PDF) studies. The results of a PDF refinement for Al_2O_3 standard are presented and compared with data acquired at a beamline of the Advanced Photon Source, where it is common to perform this type of experiment. A preliminary characterization of the $Pb_{1-x}La_xZr_{0.40}Ti_{0.60}O_3$ ferroelectric system, with x = 0.11, 0.12 and 0.15, is also shown.

1. Introduction

The atomic pair distribution function (PDF) method was developed in the 1930s (Warren *et al.*, 1936; Dalba, 2016) and has had a resurgence in recent decades as a result of new technologies and capabilities of neutron and synchrotron radiation sources (Egami & Billinge, 2003). It provides structural information of short- and medium-range order from experimental total scattering data of X-rays or neutrons by polycrystalline or amorphous samples. This method takes into account both the Bragg diffraction and diffuse scattering (which is related to the effects of short-range order). This sensitivity to local structure qualifies the PDF analysis as an ideal method for structural studies of amorphous or disordered crystalline materials. Recently, this type of analysis has also been applied successfully on polycrystalline nanometric materials that are intrinsically disordered (*i.e.* when the local structure is well defined but the long-range order is limited to a few nanometers, the size of the sample). Such structures cannot be completely captured by a conventional analysis of powder diffraction data.

This work reports on the characterization of the X-ray diffraction and spectroscopy (XDS–W09A) beamline at the Brazilian Synchrotron Light Laboratory (LNLS) (Lima *et al.*, 2016) for performing PDF studies. The performance of this beamline is illustrated by the study of alumina standards [Al_2O_3; NIST standard reference material 676 (NIST, 2005)]. The alumina was also measured at the dedicated 11-ID-B beamline of the Advanced Photon Source (APS, Argonne, USA) for comparison purposes. In addition, a preliminary PDF study on the $Pb_{1-x}La_xZr_{0.40}Ti_{0.60}O_3$ (PLZTx.100), with x = 0.11, 0.12 and 0.15, ferroelectric system was performed.

The PLZT family was previously characterized by X-ray absorption, X-ray diffraction, Raman spectroscopy and

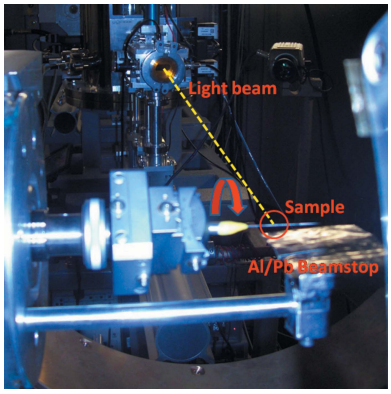

impedance spectroscopy (Mesquita *et al.*, 2010, 2012, 2014). The samples with x = 0.12 and 0.15 present a slight displacement of the dielectric permittivity (ε') curve with frequency, and can therefore be characterized as relaxors (Mesquita *et al.*, 2010). On the other hand, PLZT11 presents typical characteristics of a sample located at the limit between the normal/relaxor ferroelectric. The dielectric behavior of this sample shows a normal phase transition without dispersion, in the maximum dielectric permittivity (T_{max} = 500 K) with different frequency values (Mesquita *et al.*, 2010). The three samples present a structural phase transition from a low-temperature tetragonal phase (space group *P*4*mm*, No. 99) to a high-temperature cubic phase (space group $Pm\bar{3}m$, No. 221). At room temperature all the samples are in a tetragonal phase (Mesquita *et al.*, 2010).

2. Experimental details

2.1. XDS beamline

In this section we will describe briefly the optics and the main characteristics of the XDS beamline of the LNLS (Lima *et al.*, 2016). The storage ring of LNLS operates at 1.37 GeV (Craievich & Rodrigues, 1997; Rodrigues *et al.*, 1998). The XDS beamline was designed to take advantage of a 4 T superconducting multipole wiggler (SMW) inserted in the storage ring. This multipurpose beamline is employed for X-ray diffraction (XRD) and X-ray absorption spectroscopy (XAS) in the energy range between 5 and 30 keV. The beamline operates with a collimating mirror (VCM) with a bender (with Si, Rh and Pt stripes), a double-crystal monochromator (DCM) with interchangeable sets of crystals [plane Si(111), sagittal focusing Si(111) and plane Si(311)], and a variable-focusing mirror (VFM) with three stripes (toroidal Rh, plane Rh and toroidal Pt) with a bending mechanism to allow focus adjustments.

The following configuration was found to be the most appropriate one for performing the total scattering experiments. The VCM is set at the Rh cylindrical stripe. The DCM consists of two Si(111) crystals, where the second one is sagittally bent. Finally, the VFM is also set at the Rh cylindrical stripe. With this configuration we obtain high photon flux [photon flux $\simeq 10^{13}$ photons s^{-1} $(100\ mA)^{-1}$] at 20 keV with a spot of 2.7 mm × 0.2 mm (horizontal × vertical), reaching $Q_{max} \simeq 20$ Å^{-1} at the highest attainable diffraction angle 2θ = 165°. To perform a PDF analysis it is necessary to reach high momentum transfer (Q), preferably higher than 20 Å^{-1} (ideally 40 Å^{-1} or more); however, many successful experiments with synchrotron radiation reaching only a Q-value of 20 Å^{-1} and inhouse equipment employing Mo (18 Å^{-1}) and Ag (22 Å^{-1}) anodes have also been reported (Haverkamp & Wallwork, 2009; Ingham, 2015; Petkov, 2012; Dykhne *et al.*, 2011).

Inside the experimental hutch a low magnetic 6+2 circle Huber diffractometer is located over a translating table. The sample can be measured at different atmospheres and temperatures using a commercial closed-cycle He cryostat (Advanced Research Materials; 10–450 K), a commercial furnace (Anton Paar HTK 1200N Oven-Chamber, 300–1200 K), a hot blower (FMB Oxford, room temperature to 1273 K) and a Cryojet (Oxford, 80–500 K). More details about the beamline are given by Lima *et al.* (2016).

2.2. Standards characterization

We measured the alumina standard (Al_2O_3; NIST 676) inside 0.3 mm borosilicate glass capillary tubes at the XDS beamline. The data were collected in Debye–Scherrer geometry at room temperature, with a point scintillator detector located after a (0002) highly oriented pyrolitic graphite (HOPG) analyzer. In this configuration, unwanted background arising from external sources and Compton scattering is minimized. The employed wavelength (λ) was 0.6199 Å (20 keV). The samples were measured in a 2θ range between 1° and 165°, Q_{max} = 20.0 Å^{-1} [$Q = 4\pi \sin(\theta)/\lambda$]. The data were normalized for incoming beam intensity, employing a monitor detector to count a fixed number of photons for each angle. The experimental configuration is shown in Fig. 1.

We also measured the alumina standard using a Mythen linear detector (Bergamaschi *et al.*, 2010; Schmitt *et al.*, 2003, 2004) with the same experimental parameters given above. In this experiment, the highest diffraction angle was 150° (Q_{max} = 19.5 Å^{-1}). The use of Mythen detectors in total scattering experiments to be analyzed by the PDF technique was previously reported by Haverkamp & Wallwork (2009) measuring at 21 keV in the Australian Synchrotron. They proved that the Mythen detectors are adequate for performing these experiments.

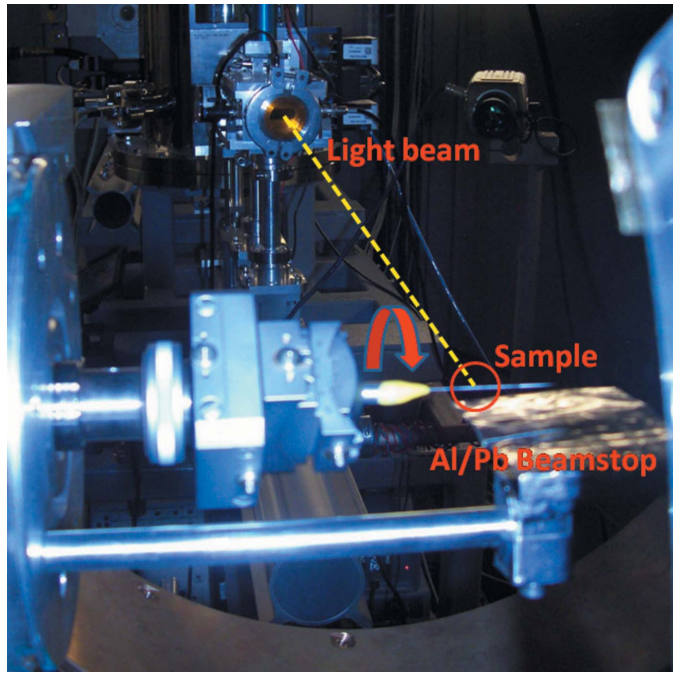

Figure 1
XDS beamline experimental setup. The samples were mounted inside the capillary tube. They rotate on their own axis, in the direction perpendicular to the beam and the scintillator.

Table 1
Differences between the measurements of alumina performed at the XDS beamline of the LNLS and the 11-ID-B beamline of the APS.

	XDS @ LNLS		
	Point (scintillator)	Linear (Mythen)	11-ID-B @ APS
Geometry	Debye–Scherrer		Transmission
Capillary	Borosilicate glass		Kapton
Wavelength (Å)	0.6199		0.143
Q_{max} (Å^{-1})	20	19.5	34
Collection time (min)	~180	35	3
Detector	HOPG + scintillator	Mythen	Plate at 18 cm
Temperature	Room temperature		
Pressure	Atmospheric		

In order to validate our experimental data acquired at LNLS we measured the same Al_2O_3 standard at the 11-ID-B beamline of the APS. The sample was located inside a polyimide tube. The experiment was performed at room temperature employing a wavelength of 0.143 Å. The XRD patterns were collected in transmission mode with a two-dimensional detector (plate) located at a distance of 18 cm. With this geometry and wavelength, Q_{max} reached 34 Å^{-1}. In addition to the Al_2O_3 patterns adquired at both beamlines, we also measured the empty capillary (background), under the same experimental conditions (angular range, beamstop position, number of photons, number of scans) in order to subtract it from the sample data during the conversion process.

In Table 1 we summarize the three distinct experimental conditions used to collect data for Al_2O_3.

2.3. Experimental procedure to characterize PLZT

The PLZTx.100 samples were prepared by the conventional mixed oxide method and a conventional sintering route. The details of the synthesis are presented elsewhere (Mesquita *et al.*, 2012). The samples were measured at the XDS beamline employing a wavelength of 0.61992 Å, and the data were normalized for the incoming beam intensity, employing a monitor.

PLZT11 is a normal ferroelectric and the diffractograms were measured at 303 K and 673 K (below and above T_{max}) employing an HTK 1200N Oven-Chamber. Both measurements were performed inside the oven using Bragg–Brentano geometry. For the other two samples (x = 0.12 and 0.15) the X-ray patterns were collected at room temperature outside the oven. In all cases, the background was measured under the same experimental conditions.

2.4. Data processing and analysis

The acquired and normalized patterns were converted into the reduced pair distribution function [$G(r)$] using the *PDFgetX3* software (Juhás *et al.*, 2013). This Python-based software uses an *ad hoc* data correction method, where the slowly changing structure-independent signal is filtered out to obtain X-ray intensities that contain structure information. Corrections performed by *PDFgetX3* include, for example, for incoherent Compton scattering, background scattering from the sample container/air, sample self-absorption, polarization of the X-ray beam, *etc*. More information about the correction in total scattering experiment data to be converted in the PDF are given by Egami & Billinge (2003; ch. 5) and Billinge & Farrow (2013).

To fit the experimental $G(r)$ obtained after processing with *PDFgetX3*, we employed the *PDFfit2–PDFgui* package (Farrow *et al.*, 2007). We fitted all the structural parameters, maintaining the symmetry of the compound. We also adjusted the scale factor, the Gaussian dampening factor (Q_{damp}) and the peak broadening. The r-dependence of the peak broadening ($\sigma_{i,j}$) was modeled using the expression (Farrow *et al.*, 2007)

$$\sigma_{i,j} = \sigma'_{i,j}\left(1 - \frac{\delta_1}{r_{i,j}} - \frac{\delta_2}{r_{i,j}^2} + Q_{broad}^2 r_{i,j}^2\right)^{1/2}, \quad (1)$$

where Q_{broad} is the PDF peak broadening from the increased intensity noise at high Q-value, and this contribution was not considered in our analysis. In the standard samples we fitted the coefficient for the $(1/r^2)$ contribution to the peak sharpening (δ_2). In the case of the data of PLZT11 collected at 673 K, we fitted the data using the coefficient δ_1 [contribution $(1/r)$] to describe the peak sharpening. The use of this coefficient is recommended for high-temperature measurements (Farrow *et al.*, 2007).

3. Results

3.1. Alumina (Al_2O_3)

From the three experiments, reduced PDF data of alumina could be fitted under the expected $R\bar{3}c$ space group (No. 167). The experimental data with their corresponding fits, for the measurements carried out at LNLS (point and linear detectors) and APS, are shown in Fig. 2. The refined cell parameters are close to the NIST values (a = 4.7592 Å and c = 12.9918 Å) (NIST, 2005).

In Fig. 3 we present selected regions of the PDF curves of Al_2O_3 to compare the three experiments. It is evident that in all cases the data are well described by the model. The real-space resolution of the curve measured at the APS is greater than the others performed at LNLS, as expected from the larger Q_{max} values measured in the APS experiment. The real-space resolution is defined as: $\delta r = 2\pi/Q_{max}$ (Petkov, 2012). The calculus of δr reveals that our measurements performed at LNLS have about half the resolution of the one performed at APS. The real-space resolution is important in cases where subtle structure features are in the range of the resolution δr. For example, Petkov *et al.* (1999) reported different Ga—As and In—As distances in (Ga–In)As semiconductor, which could only be detected due to the high real-space resolution of their experiment. On the other hand, experiments with moderate real-space resolution can be useful in many cases. For instance, in the characterization of pharmaceutical products it was demonstrated that data with Q_{max} above 12.5 Å^{-1} could be used as a fingerprint (Dykhne *et al.*, 2011).

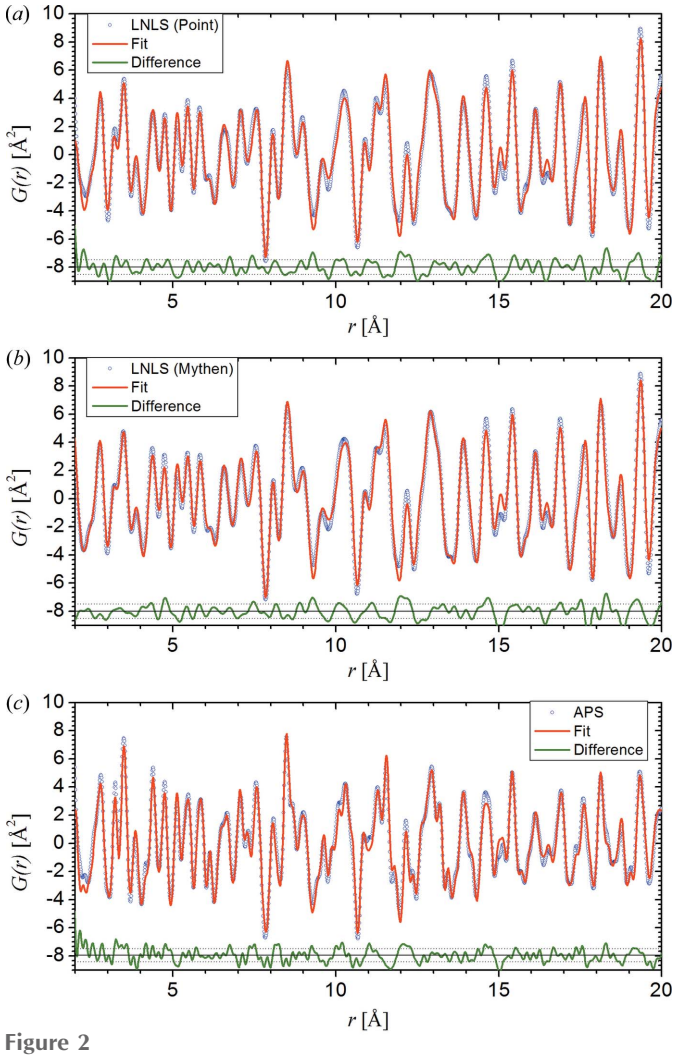

Figure 2
PDF of alumina standard measured at: (*a*) XDS @ LNLS point detector, (*b*) XDS @ LNLS Mythen detector and (*c*) 11-ID-B @ APS. Experimental data (circles) and calculated (solid red line) $G(r)$ after the structural refinement. Below the curve, with an offset for ease of viewing, the difference (solid green line), the mean value (solid black line) and the standard deviation (dashed line) of the difference are shown.

For example, PDF studies of organic compounds were successfully performed with Q_{max} values close to 20 Å^{-1} (Prill *et al.*, 2016) and with silver radiation (Petkov *et al.*, 2013).

In Table 2 we summarize the crystallographic parameters, the reduced χ^2 and R_w from the fit of the experimental PDF data.

In order to study the mesoscale region (with the data measured at LNLS), we show in Fig. 4 the calculated $G(r)$ curves for Al_2O_3 in the region 150 Å $\leq$ 200 Å, using structural parameters obtained from the fits in the low-r region (1.5–30 Å), and a comparison with the experimental $G(r)$ curve in the same r-range. We can observe that the structural parameters obtained at low r-value (Table 2) can correctly model the atomic pairs correlations up to at least the mesoscale. In fact, this result is expected in a standard sample, in which the long-range-ordered structure coincides with the short-range structure. This result shows that the setup employed at the XDS beamline can be used to obtain high-quality PDF curves

Table 2
Result of the fits for alumina measured at LNLS and APS.

Alumina: $R\bar{3}c$ (hexagonal setting); cell parameters reported by NIST: a = 4.7592 (4) Å and c = 12.9918 (2) Å.

	XDS @ LNLS		
	Point	Linear (Mythen)	11-ID-B @ APS
δ_2 (Å^{-2})	0.570	0.560	0.566
a (Å)	4.7624 (2)	4.7624 (2)	4.7638 (2)
c (Å)	13.004 (2)	13.004 (2)	13.004 (2)
Al: z	0.3524 (1)	0.3524 (1)	0.3522 (1)
O: x	0.6951 (1)	0.6949 (1)	0.6942 (1)
Al: U	0.00257 (5)	0.00267 (6)	0.00194 (5)
O: U	0.0042 (1)	0.0046 (1)	0.0028 (1)
Reduced χ^2	0.2909	0.2852	0.1693
R_w	0.1673	0.1630	0.1828

up to high r-values, which in turn can be used to investigate the structural coherence of materials of interest up to the mesoscale.

By comparing the PDFs with a high value of r, it can be observed that the LNLS (scintillator) data have better quality for $r \geq 30$ Å than those measured at the APS (Fig. 5), despite the low spatial resolution (r-space) and the high measurement time (hours *versus* minutes). The APS data, at least in this configuration, are most affected by signal dampening at high r-value, while the PDF measured at LNLS has no damping up to at least 200–300 Å. This is due to the procedure used in collecting the data. A short sample-to-detector distance (18 cm in our experiment) is used to reach high Q-space, and consequently high Q_{max}, needed for PDF studies. This geometry spoils the resolution of the diffraction data in Q-space, which leads to a widening of the diffraction peaks, producing a decay (without physical sense) in the $G(r)$ func-

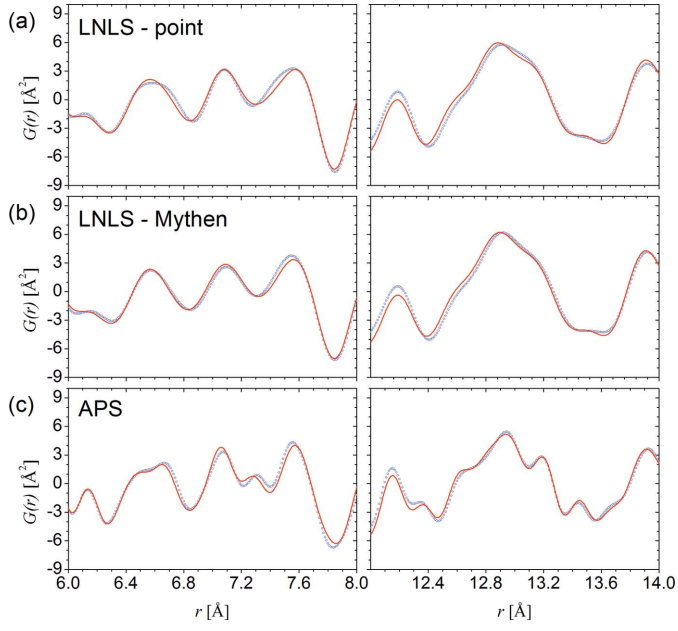

Figure 3
Comparison of the PDF data of Al_2O_3, taken at LNLS with (*a*) scintillator and (*b*) Mythen detectors, and (*c*) taken at APS. Experimental (circle) and refined (solid line) PDF of Al_2O_3.

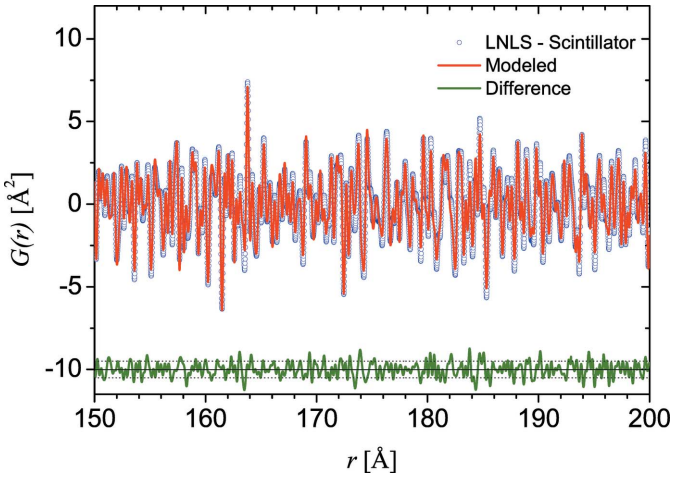

Figure 4
High *r*-region (150 Å $\leq r \leq$ 200 Å) PDF curve of alumina. Experimental curve compared with the modeled curve using parameters obtained in the low *r*-region (see Table 2). Experimental data (circles) and modeled (solid red line). Below the curve, with displacement for easy visualization, the difference (solid green line), the main value (solid black line) and the standard deviation (dotted line) of the difference are presented. The curves were scaled according to the scale factor obtained in the PDF fitting.

tion. In contrast, a configuration with a point detector and relatively narrow resolution slits (typically ∼0.5 mm, positioned 1 m from the sample) allows much higher resolution in Q. This allows for improved resolution in reciprocal space. These peaks give a PDF with more (physical) oscillations, that is, the presence of a larger number of coordinating spheres, which allows larger interatomic distances (long range) to be studied (Brühne *et al.*, 2005; Petkov, 2012). The *PDFgui* program allows modeling the damping by a Gaussian $Q_{\rm damp}$ damping coefficient. The Gaussian envelope has the following expression (Farrow *et al.*, 2007),

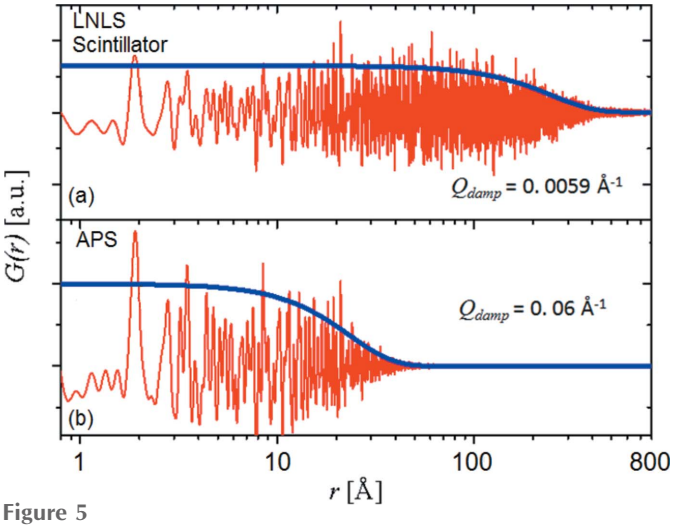

Figure 5
G(r) for the data acquired at (*a*) LNLS with the scintillator detector and (*b*) APS up to high *r*-value. It can be seen that the APS data have better quality at low *r*-value, while LNLS data have better quality at high *r*-value, because of the higher dampening factor of the APS measurement. The blue line is the damping factor modeled by equation (2).

$$B(r) = \exp\left[-\left(r\,Q_{\rm damp}\right)^2/2\right]. \qquad (2)$$

The obtained values for $Q_{\rm damp}$ are 0.0059 Å^{-1} and 0.06 Å^{-1} for the alumina collected at LNLS and APS, respectively.

3.2. $Pb_{1-x}La_xZr_{0.40}Ti_{0.60}O_3$ ferroelectric system

The conventional XRD data analysis confirms that at room temperature the three samples are tetragonal. Also, the XRD data show that PLZT11 changes its structure from tetragonal at 303 K to cubic at 673 K. In Fig. 6 we show the reflections (200), (220) and (222) of the cubic phase. We choose these particular reflections split in dissimilar ways for the possible variants of the perovskite structure.

In the data collected at room temperature the (200) and (220) regions are split into two peaks for all studied samples, and this is a good demostration that the samples crystallized in the tetragonal phase, as is expected from the ferroelectric behavior reported by Mesquita *et al.* (2010). In the high-temperature data of PLZT11 the split peaks collapse into a unique one, indicating that the sample changes its average structure to a cubic unit cell.

The room-temperature PDF curves of the relaxor samples (PLZT12 and PLZT15) reveal that the samples are tetragonal, and crystallize in the non-centrosymmetric space group *P4mm*. These curves are presented in Figs. 7(*a*) and 7(*b*); the reduced χ^2 and $R_{\rm w}$ agreement factors are inserted in the graph. The PDF fits at room temperature show a tetragonal structure with cell parameters similar to those obtained by the Rietveld method. Both relaxor samples have a $T_{\rm max}$ greater

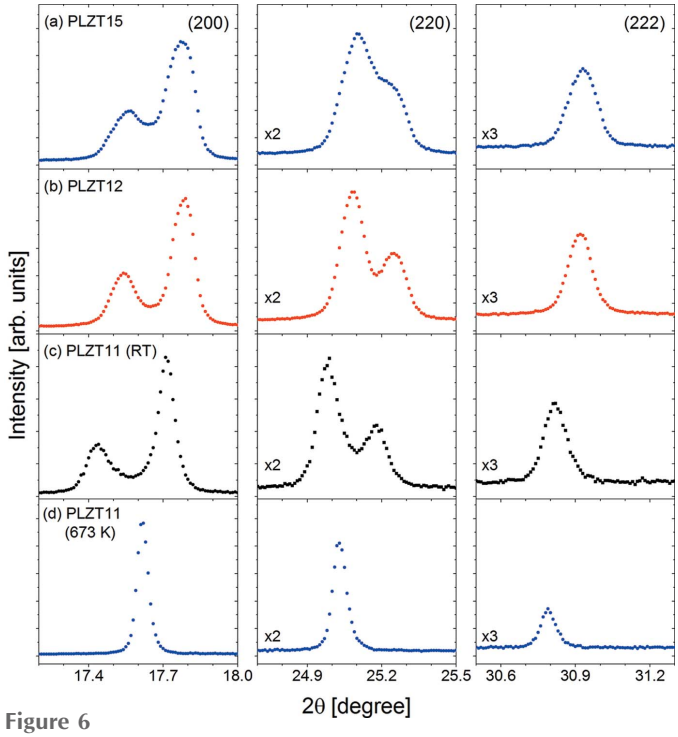

Figure 6
XRD data of the PLZT series collected at room temperature. (*a*) PLZT15, (*b*) PLZT12 and (*c*) PLZT11. (*d*) XRD data of PLZT11 at 673 K, for λ = 0.61992 Å.

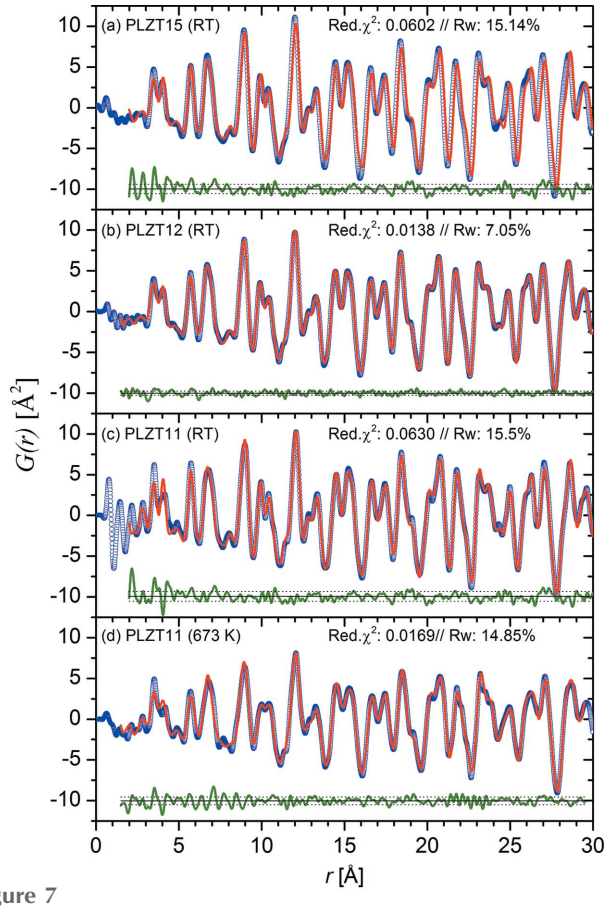

Figure 7
PDF curves of (*a*) PLZT15 at room temperature, (*b*) PLZT12 at room temperature, (*c*) PLZT11 at room temperature and (*d*) PLZT11 at 673 K. Experimental: blue circles; cubic and/or tetragonal model: red line. Measurements at room temperature were modeled with a non-centrosymmetric tetragonal *P*4*mm* cell, and the PLZT11 at 673 K was fitted with a cubic $Pm\bar{3}m$ structure. We include the reduced χ^2 and the R_w values.

than 300 K and Burn's temperature (T_B) greater than 300 K. The displacements for Ti of the special position of the cubic cell are similar. The values obtained are 0.16 (2) Å and 0.17 (2) Å for the samples with x = 0.12 and 0.15, respectively.

The study of the data of PLZT11 acquired at temperatures below and above T_{max} are presented in Figs. 7(*c*) and 7(*d*), respectively. These curves were modeled with a cubic model ($Pm\bar{3}m$) at high temperature and a non-centrosymmetric tetragonal model (*P*4*mm*). The data taken at 303 K (below T_{max}) were better fitted with a polar tetragonal model (R_w^C = 0.2267 > R_w^T = 0.1550) in accordance with the data obtained by Rietveld analysis. The displacement of the atoms from cubic symmetry is 0.17 (2) Å. On the other hand, the high-temperature data (T = 673 K, above T_{max}) could be well described by a non-polar cubic model, and a tetragonal model did not improve the fit significantly. The cell parameters obtained are practically equivalent, the difference being within experimental error. The non-centrosymmetric tetragonal symmetry allows the movement of atoms in the z direction and the analysis of such displacements also shows they are null, within experimental error. This is good and strong evidence that the fit made with the tetragonal model is not adequate. This can be explained because the measurement was performed at temperatures higher than T_B, which is the temperature where the ferroelectric material starts to present randomly polarized nano-regions (Burns & Dacol, 1983).

4. Conclusions

In summary, the XDS beamline at LNLS has been successfully set up and tested to perform total scattering experiments to be analyzed by PDF. This technique allows the LNLS to increase its capability in characterization of nano-sized materials and in systems where the local order dominates their physical properties, such as, for example, ferroelectric materials. The different setups already available at this beamline allow PDF studies to be performed on a broad range of materials, which may be carried out under different sample environments and temperatures. The use of this facility has been demonstrated by an investigation of a standard sample (Al_2O_3) and also comparing the data obtained at LNLS with data collected at the APS. Nowadays, PDF studies of materials using the XDS beamline are under the reach of external users.

Also, the PDFs of the PLZT family were studied. The relaxor samples were modeled with a tetragonal cell at room temperature. We have obtained the expected structures of PLZT11 at 303 K and 673 K, tetragonal and cubic, respectively.

Acknowledgements

The authors acknowledge the LNLS (XRD1-16082 and XRD1-16982) and APS (GUP-40487) for the beam time. We thank the staff of the XDS and the 11-ID-B beamlines, especially Dr Karena Chapman and Dr Olaf Borkiewicz (APS) for the measurement of the alumina standard at APS. Also, the authors are grateful to Professor Dr Valeri Petkov for fruitful discussions and Dr Frederico Alves-Lima for assitance during the measurement at the XDS beamline. This work was supported by FAPESP (Processes 2013/02160-5 and 2012/04870-7) and CNPq, Brazil.

References

Bergamaschi, A., Cervellino, A., Dinapoli, R., Gozzo, F., Henrich, B., Johnson, I., Kraft, P., Mozzanica, A., Schmitt, B. & Shi, X. (2010). *J. Synchrotron Rad.* **17**, 653–668.
Billinge, S. J. L. & Farrow, C. L. (2013). *J. Phys. Condens. Matter*, **25**, 454202.
Brühne, S., Uhrig, E., Luther, K.-D., Assmus, W., Brunelli, M., Masadeh, A. S. & Billinge, S. J. L. (2005). *Z. Kristallogr.* **220**, 962–967.
Burns, G. & Dacol, F. H. (1983). *Phys. Rev. B*, **28**, 2527–2530.
Craievich, A. F. & Rodrigues, A. R. D. (1997). *Braz. J. Phys.* **27**, 417–424.
Dalba, G. (2016). *Acta Cryst.* A**72**, 591–607.
Dykhne, T., Taylor, R., Florence, A. & Billinge, S. J. L. (2011). *Pharm. Res.* **28**, 1041–1048.
Egami, T. & Billinge, S. (2003). Editors. *Underneath the Bragg Peaks: Structural Analysis of Complex Materials*, 1st ed. Amsterdam: Pergamon.

Farrow, C. L., Juhas, P., Liu, J. W., Bryndin, D., Božin, E. S., Bloch, J., Proffen, T. & Billinge, S. J. L. (2007). *J. Phys. Condens. Matter*, **19**, 335219.
Haverkamp, R. G. & Wallwork, K. S. (2009). *J. Synchrotron Rad.* **16**, 849–856.
Ingham, B. (2015). *Crystallogr. Rev.* **21**, 229–303.
Juhás, P., Davis, T., Farrow, C. L. & Billinge, S. J. L. (2013). *J. Appl. Cryst.* **46**, 560–566.
Lima, F. A., Saleta, M. E., Pagliuca, R. J. S., Eleotério, M. A., Reis, R. D., Fonseca Júnior, J., Meyer, B., Bittar, E. M., Souza-Neto, N. M. & Granado, E. (2016). *J. Synchrotron Rad.* **23**, 1538–1549.
Mesquita, A., Mastelaro, V. & Michalowicz, A. (2010). *Phase Trans.* **83**, 251–262.
Mesquita, A., Michalowicz, A. & Mastelaro, V. R. (2012). *J. Appl. Phys.* **111**, 104110.
Mesquita, A., Michalowicz, A., Pizani, P., Provost, K. & Mastelaro, V. (2014). *J. Alloys Compd.* **582**, 680–687.
NIST (2005). Standard Reference Material 676. NIST, Gaithersburg, MD, USA (https://www-s.nist.gov/srmors/view_detail.cfm?srm=676).
Petkov, V. (2012). *Characterization of Materials*, pp. 1361–1372. New York: Wiley.
Petkov, V., Jeong, I.-K., Chung, J. S., Thorpe, M. F., Kycia, S. & Billinge, S. J. L. (1999). *Phys. Rev. Lett.* **83**, 4089–4092.
Petkov, V., Ren, Y., Kabekkodu, S. & Murphy, D. (2013). *Phys. Chem. Chem. Phys.* **15**, 8544–8554.
Prill, D., Juhás, P., Billinge, S. J. L. & Schmidt, M. U. (2016). *Acta Cryst.* A**72**, 62–72.
Rodrigues, A. R. D., Craievich, A. F. & Gonçalves da Silva, C. E. T. (1998). *J. Synchrotron Rad.* **5**, 1157–1161.
Schmitt, B., Brönnimann, C., Eikenberry, E., Gozzo, F., Hörmann, C., Horisberger, R. & Patterson, B. (2003). *Nucl. Instrum. Methods Phys. Res. A*, **501**, 267–272.
Schmitt, B., Brönnimann, C., Eikenberry, E., Hülsen, G., Toyokawa, H., Horisberger, R., Gozzo, F., Patterson, B., Schulze-Briese, C. & Tomizaki, T. (2004). *Nucl. Instrum. Methods Phys. Res. A*, **518**, 436–439.
Warren, B. E., Krutter, H. & Morningstar, O. (1936). *J. Am. Ceram. Soc.* **19**, 202–206.